




Cite this: *Chem. Commun.*, 2021, 57, 11859

Received 15th August 2021,
Accepted 7th October 2021

DOI: 10.1039/d1cc04501f

rsc.li/chemcomm

A high dimensional oxysulfide built from large iron-based clusters with partial charge-ordering†

Batoul Almoussawi,  Angel M. Arevalo-Lopez,  Pardis Simon  and Houria Kabbour  *

Herein we report the original $\text{Ba}_{10}\text{Fe}_{7.75}\text{Zn}_{5.25}\text{S}_{18}\text{Si}_3\text{O}_{12}$ oxysulfide which crystallizes in a new structural type. Contrary to the usual oxychalcogenides, it crystallizes with a non-centrosymmetric 3D spatial network structure built from large magnetic clusters consisting of twelve $(\text{Fe}^{2+/3+}/\text{Zn})\text{S}_3\text{O}$ tetrahedra decorating a central Fe^{2+}S_6 octahedron and exhibiting a spin glass state.

Mixed anion compounds frequently contain transition metals in unusual chemical environments and states due to heteroleptic coordination. These may lead to fascinating properties¹ with new perspectives opened in several fields such as superconductors.^{2,3} Among them, Fe-based pnictide or chalcogenide layers have attracted much attention. Synthetic strategies based on mixed anion chemistry have given access to original phases⁴ and attractive physical properties.⁵ It has also led to enhanced performances in various fields of application such as photocatalysis or ionic conductivity.⁶ In this context, oxychalcogenides are increasingly investigated for diverse applications such as non-linear optics⁷ or thermoelectrics⁸ and are also emerging as visible light water-splitting photocatalysts.^{9–11} It is well established that oxychalcogenides tend to form layered structures, which is detailed in several reviews.^{8,12,13} This is favored by the very different ionic radii and electronegativities of O^{2-} ($\chi = 3.44$) and S^{2-} ($\chi = 2.58$) which arrange in distinct layers. Specific cation–anion affinities also influence the structural arrangement. A soft cation (more polarisable) and a hard cation (less polarisable) would prefer

to bond to the larger chalcogenide and the smaller oxide anions, respectively. Such distinct layers can be defined as 2D building blocks. This has allowed the prediction of new functional compounds by stacking complementary layers of distinct chemical nature.^{14,15} The polar layered oxysulfide CaOFeS , a member of a family including non-linear optical materials, exhibits uncommon heteroleptic FeS_3O tetrahedra and was investigated for magnetodielectric and photovoltaic effects.^{16,17} Other peculiar electronic and magnetic behaviors^{18–20} are found among oxychalcogenides. For instance, spin-glass behavior promoted by mixed anion interactions has been observed in the layered oxysulfides $\text{Sr}_4\text{Mn}_{2.91}\text{O}_{7.40}\text{Cu}_2\text{S}_{21}$ and $\text{Ba}_2\text{Mn}_2\text{O}_4\text{Cu}_{0.9}\text{S}$.²² Magnetic frustration is a required ingredient for the observation of exotic quantum states.^{23–25} These are often studied in 3D oxides with corner sharing tetrahedral lattices such as spinels²⁶ or pyrochlores.²⁷ Apart from oxides, the fluoride CsFe_2F_6 ²⁸ pyrochlore and the In-diluted thiospinel $\text{CdCr}_{2x}\text{In}_{2(1-x)}\text{S}_4$ ^{29,30} are spin-glass materials. In the $\text{Bi}_{1.8}\text{Fe}_{1.2}\text{SbO}_7$ ³¹ pyrochlore, anion mixing through fluorination led to the variation of the spin glass dynamics.

We present an original oxysulfide with a non-centrosymmetric 3D-network involving corner-sharing tetrahedra. The structure is built with 0D Fe-based large magnetic clusters $\text{Fe}_{13}\text{O}_{12}\text{S}_{18}$ diluted with Zn and interconnected through silicate groups. The sulfur atoms provide intra-cluster bonding, while oxygen atoms are located on the outer shell of the clusters. The material orders into a spin-glass state at low temperature. Such 3D networks are scarce³² for oxysulfides, which are dominated by low-dimensional structures. Furthermore, the elementary building blocks are large *clusters* instead of the common *layered* building blocks found in this class of materials. While the layered character brings interesting anisotropic electronic properties, a pressure-induced 2D–3D structural transition allowed drastic enhancement of electrical conductivity and photoelectric response in the $\text{Bi}_9\text{O}_{7.5}\text{S}_6$ oxysulfide.³³ Here, the original Fe-based oxysulfide building block opens new perspectives for the design of functional phases combining oxide and chalcogenide anions in high dimensional structures.

Univ. Lille, CNRS, Centrale Lille, ENSCL, Univ. Artois, UMR 8181 – UCCS – Unité de Catalyse et Chimie du Solide, Lille F-59000, France.

E-mail: houria.kabbour@univ-lille.fr

† Electronic supplementary information (ESI) available: Experimental procedures and synthesis; Table S1 with structure solution and refinement details; Tables S2 and S3 with atomic positions and anisotropic thermal parameters; Table S4 with main distances, Table S5 with magnetic exchange path details (Fig. S4) and discussion; Vogel–Fulcher parameters (Table S6); Ba^{2+} environments (Fig. S1); Rietveld refinement (Fig. S2) and its discussion; magnetization at 2 and 300 K (Fig. S3). CCDC 2090920. For ESI and crystallographic data in CIF or other electronic format see DOI: 10.1039/d1cc04501f



The new oxysulfide phase $\text{Ba}_{10}\text{Fe}_{7.75}\text{Zn}_{5.25}\text{S}_{18}\text{Si}_3\text{O}_{12}$ was synthesized through a solid-state reaction in an evacuated sealed quartz tube (see ESI†). Its structure was solved and refined using single crystal X-ray diffraction (XRD) data (Tables S1–S3, ESI† and CCDC deposition number 2090920). The treatment of the data was performed using Jana2006³⁴ and charge flipping³⁵ for structural solution and the least squares method for refinement. This phase crystallizes in a new structural type with the unit cell parameter $a = 13.3380(1)$ Å and the non-centrosymmetric space group $I\bar{4}3m$. Centrosymmetric trials led to unreasonable solutions. Thus, inversion twinning was allowed to refine, resulting in a Flack parameter of 0.04(8), indicating that the measured crystal was single-domain. Energy dispersive X-ray analysis on single crystals led to the average atomic ratio of 23.7/16.33/13.2/7.03/39.76 for Ba/Fe/Zn/Si/S, respectively. This is in good agreement with the composition found at the end of the refinement, *i.e.* 22.7/17.6/11.9/6.8/40.9. In particular the Zn/Fe distribution was determined to 0.56(3)/0.44(3) at the Fe2 site (see Table S2, ESI†). The structure can be described as a 3D framework formed by repetitive 0D units, which are interconnected along the three crystallographic directions through Si^{4+} bridges. The Si^{4+} bridges form silicate groups having their oxygen atoms shared with the clusters.

These elementary cluster units (Fig. 1) are composed of one FeS_6 octahedron (Fig. 1b) decorated by twelve $(\text{Fe}/\text{Zn})\text{S}_3\text{O}$ heteroleptic tetrahedra (Fig. 1c) arranged into four trimers. The later arrangement defines the $(\text{Fe}_1(\text{Fe}/\text{Zn})_{12}\text{O}_{12}\text{S}_{18})$ magnetic clusters, see Fig. 1d and e. In the $(\text{Fe}/\text{Zn})\text{S}_3\text{O}$ tetrahedra, Fe2(Zn1) is coordinated to two different types of anions with $d_{\text{Fe2-S2}} = 2.311(2)$ Å, $d_{\text{Fe2-S3}} = 2.332(2)$ Å and $d_{\text{Fe2-O1}} = 1.972(6)$ Å. The anionic segregation is such that the sulfur atoms provide intra-cluster bonding, while oxygen atoms are located at the outer shell of the clusters linked through Si^{4+} bridges. The observed environments follow Pearson's HSAB theory well. Then one can explain why a 3D structure is obtained in this particular case. Considering the coordination polyhedra stable in this structure Fe^{2+}S_6 , $(\text{Fe}/\text{Zn})\text{S}_3\text{O}$ and SiO_4 , the cluster arrangement allows fulfilling the coordination preferences: FeS_6 at the core shares sulphur with the surrounding $(\text{Fe}/\text{Zn})\text{S}_3\text{O}$ which point their unique apical oxygen outside the cluster to bond with the Si^{4+} , the latter having the strongest affinity for oxygen.

Similar heteroleptic FeOS_3 are present in the layered oxysulfide CaFeSO^{16} where they share corners to build layers separated by calcium sheets; similarly, $\text{CaOZnS}^{36,37}$ contains tetrahedral ZnOS_3 . This (Fe/Zn) environment remains uncommon. It is also found in the distinct structural type of $\text{SrFe}_2\text{S}_2\text{O}^{38}$ and $\text{BaFe}_2\text{S}_2\text{O}^{39}$ with more complex layers involving both tetrahedral corner and edge sharing. The FeS_6 octahedra are connected to the tetrahedral FeOS_3 and characterized by a longer bonding distance ($d_{\text{Fe1-S2}} = 2.559(3)$ Å) than in FeOS_3 ($d_{\text{Fe2-S2}} = 2.311(2)$ Å, $d_{\text{Fe2-S3}} = 2.332(2)$ Å) consistent with the calculated Fe^{2+} oxidation state. Regarding the mean oxidation state $\text{Fe}^{+2.26}$ in the phase, it is consistent with the charge distribution deduced from the XPS and magnetic analysis shown later. The clusters are separated by SiO_4 (Fig. 1f) groups by sharing all oxygen corners of $(\text{Fe}/\text{Zn})\text{S}_3\text{O}$ with $d_{\text{Si1-O1}} = 1.628(5)$ Å. Each silicate group is connected to two different clusters. Ba^{2+} are located in the voids and their arrangement is shown and discussed in Fig. S1 (ESI†).

A high purity powder could be obtained from the refined composition after many synthetic efforts. The Rietveld refinement based on the single crystal structure model converged with the unit cell parameter $a = 13.3350(1)$ Å and the reliability factors $R_{\text{obs}} = 0.0323$, $wR_{\text{obs}} = 0.0384$, $R_{\text{all}} = 0.0328$, $wR_{\text{all}} = 0.0388$ and $\text{GOF} = 3.29$. The results are consistent with the single crystal data (see Fig. S2 and Tables S6 and S7, ESI†). A few low intensity peaks are found with the majority phase and could not be indexed with certainty with any existing phase. They do not indicate any straightforward symmetry change compared to the single crystal refinement either. Nevertheless, regarding the minor contribution of those peaks, we used our highest purity powder for the physical measurements considering the presence of a minor impurity for the interpretation.

In order to confirm the presence of both charges in $(\text{Fe}^{2+/3+})\text{S}_3\text{O}$ tetrahedra and the general Fe charge distribution, the Fe 2p core level spectrum was examined. Reference data were taken on both vacuum fractured pyrrhotite (Fe_7S_8) and air-oxidized pyrrhotite as reported by Pratt *et al.*⁴⁰ In this study, Fe_7S_8 multiplet structure was generated based on theoretical *p* core level multiplet structures for free transition metal ions calculated by Gupta and Sen⁴¹ and compared with the work of McIntyre and Zetarik⁴² on Fe(II) and Fe(III) ions in iron oxides. The calculated integrated envelope (red line) is a reasonable fit

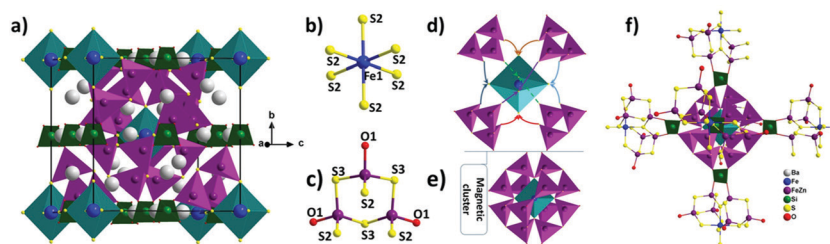


Fig. 1 (a) View of the unit cell of $\text{Ba}_{10}\text{Fe}_{7.75}\text{Zn}_{5.25}\text{S}_{18}\text{Si}_3\text{O}_{12}$. (b) The octahedra FeS_6 . (c) Three heteroleptic tetrahedra FeS_3O connected by sharing S3, (d) connection of (b) and (c). (e) The magnetic cluster $\text{Fe}_1(\text{Fe}/\text{Zn})_{12}\text{O}_{12}\text{S}_{18}$ with $(\text{Fe}/\text{Zn})\text{S}_3\text{O}$ tetrahedra in purple and FeS_6 octahedra in blue. SiO_4 groups, Ba, O and S atoms are represented in green, grey, red and yellow, respectively. (f) Representation of how clusters connect each other through the (SiO_4) groups. Only the central cluster is fully represented to highlight the inter-clusters connection, Ba atoms are also omitted for clarity.



to our experimental data (Fig. 2a), thus confirming the presence of mixed cation charges $\text{Fe}^{3+}/\text{Fe}^{2+}$. The major Fe(II) peak has a binding energy of 708.6 eV, which is similar to the fitted $\text{Fe(II)}-\text{S}$ bonded peak binding energy of Fe_7S_8 reported by Pratt *et al.*, but slightly shifted to a higher binding energy. The binding energy of the main Fe(III) peak is 710.4 eV, which is similar to the fitted $\text{Fe(III)}-\text{O}$ binding energy of $\alpha\text{-Fe}_2\text{O}_3$ reported by McIntyre and Zetaruk which was 711.0 eV, although the Fe(III) peaks are slightly shifted to lower binding energies. The fact that Fe(III) peaks have been shifted to lower binding energies as compared to those observed for pure Fe(III) oxides, and that Fe(II) peaks have been shifted to higher binding energies as compared to those observed for pure Fe(II) sulfides reflects the mixed $\text{Fe}-\text{S}/\text{Fe}-\text{O}$ coordination in our system for both Fe(II) and Fe(III) species. Indeed, the percentage of the total signal derived from Fe(III) components in the spectrum is 36%, whereas the expected distribution of iron in $\text{Ba}_{10}\text{Fe}_{7.75}\text{Zn}_{5.25}\text{Si}_3\text{S}_{18}\text{O}_{12}$ corresponds to 25% of total iron with the Fe^{3+} oxidation state ($2*\text{Fe}^{3+}$ and $5.75*\text{Fe}^{2+}$; $1*\text{Fe}^{2+}$ in the octahedral site). This suggests that some Fe(II) (S or O bonded) in the near-surface has been oxidized to Fe(III) and bonded to oxygen.

Fig. 2b shows the temperature dependence of the resistivity for $\text{Ba}_{10}\text{Fe}_{7.75}\text{Zn}_{5.25}\text{Si}_3\text{S}_{18}\text{O}_{12}$ which is typical of a semiconductor. The resistivity curve can be well fitted with the relation $\rho \propto \exp\left(\frac{\Delta g}{2k_B T}\right)$, where Δg is the semiconductor band gap and k_B is the Boltzmann constant, leading to $\Delta g = 0.4$ eV. The zero field-cooled/field-cooled (ZFC/FC) magnetic measurements under a 1000 Oe field are shown in Fig. 3a and b. The ZFC exhibits a maximum of ~ 2.6 K and diverges from the FC data below this temperature. The inverse ZFC data were fit between 150 and 300 K with the Curie–Weiss law, $1/\chi = T/C - \theta_{\text{CW}}/C$, resulting in a large negative value $\theta_{\text{CW}} = -343.9$ K, indicating strong antiferromagnetic (AFM) interactions between Fe ions, and $C = 25.075$ emu K mol $^{-1}$. The effective moment $\mu_{\text{eff}} = 5.09$ μ_B/Fe shows good agreement with the expected theoretical value for the refined distribution of high spin ($S = 2$) Fe^{3+} and ($S = 5/2$) Fe^{2+} . Indeed, the calculation of the effective moment of 7.75 iron atoms per formula unit ($2*\text{Fe}^{3+}$ and $5.75*\text{Fe}^{2+}$) leads to 5.16 μ_B/Fe , close to the experimental value of 5.09. The value $|(T_{\text{CW}})/T_N| \approx 137.2$ indicates a strong frustration⁴³ close, for instance, to the frustration parameter ≈ 135 of $\text{SrGa}_{12-x}\text{Cr}_x\text{O}_{19}$.⁴⁴ The evolution of T_f as a

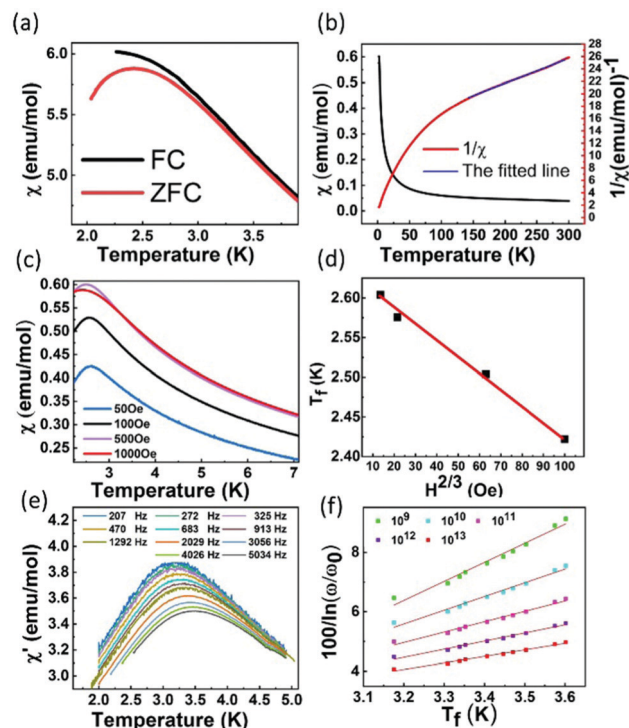


Fig. 3 (a) Zoom of ZFC/FC at low temperature. (b) ZFC/FC dc magnetic susceptibility with $1/\chi$ fitted between 150 and 300 K. (c) Evolution of T_f as a function of the applied magnetic field and (d) the Almeida–Thouless fit. (e) $\chi'(T)$ measured at several fixed frequencies. (f) Vogel–Fulcher fit with different fixed $\omega_0/2\pi$ in the typical range of 10^9 – 10^{13} Hz for spin-glass.

function of the applied magnetic field (Fig. 3c) is well-fitted with the Almeida–Thouless relation⁴⁵ (Fig. 3d) which is a good indicator of a spin-glass transition.

The AC magnetic susceptibility confirmed the spin-glass transition, as shown in Fig. 3e. The temperature dependence of the real part of the AC susceptibility at different frequencies with zero external DC magnetic field and an oscillating field of 16 Oe shows a typical temperature shift of a spin-glass. The AC susceptibility is frequency-dependent and has a nonzero imaginary component. It could be modeled by the Vogel–Fulcher law:^{46,47} $\omega = \omega_0 \exp[-E_a/k_B(T_f - T_0)]$, where ω_0 is the characteristic frequency fixed to typical values for spin-glass following reported procedures,⁴⁸ E_a is the activation energy, k_B is the Boltzmann constant, T_f is the freezing temperature and T_0 is the Vogel–Fulcher temperature that gives a measure of the interaction effect. T_f should be proportional to $1/\ln(\omega/\omega_0)$ for a spin glass. A linear variation is indeed obtained for each frequency. The fits to the data give T_0 from 1.36 K to 2.21 K (Fig. 3f and Table S8, ESI†) in good agreement with the freezing temperature found by DC. For these values, $t^* = (T_f - T_0)/T_f$ is found in the range of 0.15–0.48; t^* above 0.15 is common for cluster spin-glass materials.^{48,49}

Comparatively, the layered CaOFes and spin ladder $\text{Ba(Sr)Fe}_2\text{S}_2\text{O}$ phases described above show a partial long range AFM ordering and (canted)-AFM ordering, respectively. The behavior of CaOFes is related to its frustrated triangular sheets and shows complex magnetodielectric effects.^{16,17,50} The latter

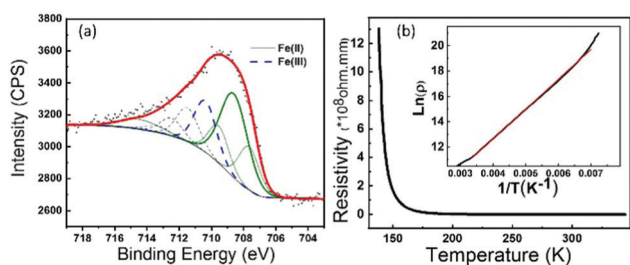


Fig. 2 (a) Fe $2p_{3/2}$ XPS spectrum of the $\text{Ba}_{10}\text{Fe}_{7.75}\text{Zn}_{5.25}\text{Si}_3\text{S}_{18}\text{O}_{12}$ sample (square symbols). The green solid lines correspond to Fe(II) (multiplets and satellite), the blue dotted lines correspond to Fe(III) (multiplet structure), and the red solid line represents the calculated integrated fit. (b) Temperature-dependent resistivity of $\text{Ba}_{10}\text{Fe}_{7.75}\text{Zn}_{5.25}\text{Si}_3\text{S}_{18}\text{O}_{12}$; $\ln(\rho)$ versus T^{-1} is fitted and shown in the inset.

phases are remarkable examples of 2D magnetic units based on FeS_3O entities. The $\text{Ba}_5\text{Fe}_{6+x}\text{S}_{4+x}\text{O}_8^{51}$ phases represent another type of oxysulfide with spin-glass members and a complex structure with distorted FeS_4O_2 and FeS_2O_4 octahedral perovskite sub-units forming tunnels partially occupied by Fe and S. In the title phase, we observe a new and remarkable arrangement of the FeS_3O tetrahedra combined to decorate one Fe^{2+}S_6 octahedron to form large magnetic clusters. Note that, distinctly, magnetic clustering is known for ions without forming distinct entities such as in the Zn-diluted frustrated lattice $\text{Zn}_3\text{V}_3\text{O}_8^{52}$ or in $\text{Ba}_9\text{V}_3\text{S}_{15}^{53}$. Despite strong AFM interactions in our phase, frustration raises from competing intra-cluster interactions and Zn disturbing magnetic exchanges.

The properties discussed above are coherent with the complex magnetic exchange paths (Fig. S4 and Table S5, ESI†) involving mixed valence. The magnetic paths J1–J6 are discussed in the ESI.† Intra-cluster magnetic interactions are mediated through sulfide anions, while weaker inter-cluster super-super-exchanges involve oxide anions.

The original cubic non-centrosymmetric oxysulfide $\text{Ba}_{10}\text{Fe}_{7.75}\text{Zn}_{5.25}\text{S}_{18}\text{Si}_3\text{O}_{12}$ shows a 3D-structure made of large diluted magnetic clusters, therefore standing apart from more commonly encountered layered oxychalcogenides. This partially charge-ordered phase presents strong AFM interactions with a spin-glass state arising from cluster geometry and disorder. It provides an exceptional new structure type and a rich playground for exotic physics.

Conflicts of interest

There are no conflicts to declare.

Notes and references

- H. Kageyama, K. Hayashi, K. Maeda, J. P. Attfield, Z. Hiroi, J. M. Rondinelli and K. R. Poeppelmeier, *Nat. Commun.*, 2018, **9**, 772.
- Y. Kamihara, T. Watanabe, M. Hirano and H. Hosono, *J. Am. Chem. Soc.*, 2008, **130**, 3296–3297.
- J. W. Lynn and P. Dai, *Phys. C*, 2009, **469**, 469–476.
- B. Almoussawi, M. Huvé, V. Dupray, S. Clevers, V. Duffort, O. Mentré, P. Roussel, A. M. Arevalo-Lopez and H. Kabbour, *Inorg. Chem.*, 2020, **59**, 5907–5917.
- T. Motohashi, M. Ito, Y. Masubuchi, M. Wakeshima and S. Kikkawa, *Inorg. Chem.*, 2012, **51**, 11184–11189.
- (a) S. Gao, T. Broux, S. Fujii, C. Tassel, K. Yamamoto, Y. Xiao, I. Oikawa, H. Takamura, H. Ubukata, Y. Watanabe, K. Fujii, M. Yashima, A. Kuwabara, Y. Uchimoto and H. Kageyama, *Nat. Commun.*, 2021, **12**, 201; (b) J. M. Hodges, Y. Xia, C. D. Malliakas, T. J. Slade, C. Wolverton and M. G. Kanatzidis, *Chem. Mater.*, 2020, **32**, 10146–10154; (c) G. J. Limburn, M. J. P. Stephens, B. A. D. Williamson, A. Iborra-Torres, D. O. Scanlon and G. Hyett, *J. Mater. Chem. A*, 2020, **8**, 19887–19897.
- Y. F. Shi, W. B. Wei, X. T. Wu, H. Lin and Q. L. Zhu, *Dalton Trans.*, 2021, **50**, 4112–4118.
- S. D. N. Luu and P. Vaqueiro, *J. Materiomics*, 2016, **2**, 131–140.
- J. Cui, C. Li and F. Zhang, *ChemSusChem*, 2019, **12**, 1872–1888.
- Q. Wang, M. Nakabayashi, T. Hisatomi, S. Sun, S. Akiyama, Z. Wang, Z. Pan, X. Xiao, T. Watanabe, T. Yamada, N. Shibata, T. Takata and K. Domen, *Nat. Mater.*, 2019, **18**, 827–832.
- H. Kabbour, A. Sayede, S. Saitzek, G. Lefèvre, L. Cario, M. Trentesaux and P. Roussel, *Chem. Commun.*, 2020, **56**, 1645–1648.
- K. Ueda, H. Hiramatsu, M. Hirano, T. Kamiya and H. Hosono, *Thin Solid Films*, 2006, **496**, 8–15.
- S. J. Clarke, P. Adamson, S. J. C. Herkelrath, O. J. Rutt, D. R. Parker, M. J. Pitcher and C. F. Smura, *Inorg. Chem.*, 2008, **47**, 8473–8486.
- L. Cario, H. Kabbour and A. Meerschaut, *Chem. Mater.*, 2005, **17**, 234–236.
- H. Kabbour, L. Cario, S. Jobic and B. Corraze, *J. Mater. Chem.*, 2006, **16**, 4165–4169.
- C. Delacotte, O. Pérez, A. Pautrat, D. Berthebaud, S. Hébert, E. Suard, D. Pelloquin and A. Maignan, *Inorg. Chem.*, 2015, **54**, 6560–6565.
- Y. Zhang, L. Lin, J.-J. Zhang, X. Huang, M. An and S. Dong, *Phys. Rev. Mater.*, 2017, **1**, 034406.
- H. Kabbour, E. Janod, B. Corraze, M. Danot, C. Lee, M. H. Whangbo and L. Cario, *J. Am. Chem. Soc.*, 2008, **130**, 8261–8270.
- J. B. He, D. M. Wang, H. L. Shi, H. X. Yang, J. Q. Li and G. F. Chen, *Phys. Rev. B: Condens. Matter Mater. Phys.*, 2011, **84**, 205–212.
- S. Tippireddy, D. S. Prem Kumar, S. Das and R. C. Mallik, *ACS Appl. Energy Mater.*, 2021, **4**, 2022–2040.
- G. Hyett, N. Barrier, S. J. Clarke and J. Hadermann, *J. Am. Chem. Soc.*, 2007, **129**, 11192–11201.
- G. Hyett, Z. A. Gál, C. F. Smura and S. J. Clarke, *Chem. Mater.*, 2008, **20**, 559–566.
- S. Kundu, T. Dey, A. V. Mahajan and N. Büttgen, *J. Phys.: Condens. Matter*, 2020, **32**, 115601.
- J. P. Sheckelton, J. R. Neilson, D. G. Soltan and T. M. McQueen, *Nat. Mater.*, 2012, **11**, 493–496.
- C. A. Bridges, T. Hansen, A. S. Wills, G. M. Luke and J. E. Greedan, *Phys. Rev. B: Condens. Matter Mater. Phys.*, 2006, **74**, 1–9.
- M. C. Kemei, P. T. Barton, S. L. Moffitt, M. W. Gaultois, J. A. Kurzman, R. Seshadri, M. R. Suchomel and Y. Il Kim, *J. Phys.: Condens. Matter*, 2013, **25**, 326001.
- A. F. Fuentes, K. Boulahya, M. Maczka, J. Hanuza and U. Amador, *Solid State Sci.*, 2005, **7**, 343–353.
- S. Liu, Y. Xu, Y. Cui, J. Wang, K. Sun, S. Yu and X. Hao, *J. Phys.: Condens. Matter*, 2017, **29**, 315501.
- E. Vincent and V. Dupuis, *Springer Ser. Mater. Sci.*, 2018, **275**, 31–56.
- E. Vincent, J. Hammann and M. Ocio, *J. Stat. Phys.*, 2009, **135**, 1105–1120.
- A. V. Egorysheva, O. G. Ellert, O. M. Gaitko, M. N. Brekhovskikh, I. A. Zhidkov and Y. V. Maksimov, *Inorg. Mater.*, 2017, **53**, 962–968.
- A. Meerschaut, A. Lafond, P. Palvadeau, C. Deudon and L. Cario, *Mater. Res. Bull.*, 2002, **37**, 1895–1905.
- G. Zhang, Q. Zhang, Q. Hu, B. Wang and W. Yang, *J. Mater. Chem. A*, 2019, **7**, 4019–4025.
- V. Petříček, M. Dušek and L. Palatinus, *Z. Kristallogr. - Cryst. Mater.*, 2014, **229**, 345–352.
- A. van der Lee, *J. Appl. Crystallogr.*, 2013, **46**, 1306–1315.
- T. Sambrook, C. F. Smura, S. J. Clarke, K. M. Ok and P. S. Halasyamani, *Inorg. Chem.*, 2007, **46**, 2571–2574.
- S. A. Petrova, V. P. Mar'evich, R. G. Zakharov, E. N. Selivanov, V. M. Chumarev and L. Y. Udova, *Dokl. Chem.*, 2003, **393**, 255–258.
- H. Guo, M.-T. Fernández-Díaz, A. C. Komarek, S. Huh, P. Adler and M. Valldor, *Eur. J. Inorg. Chem.*, 2017, 3829–3833.
- M. Valldor, P. Adler, Y. Prots, U. Burkhardt and L. H. Tjeng, *Eur. J. Inorg. Chem.*, 2014, 6150–6155.
- A. R. Pratt, I. J. Muir and H. W. Nesbitt, *Geochim. Cosmochim. Acta*, 1994, **58**, 827–841.
- R. P. Gupta and S. K. Sen, *Phys. Rev. B: Condens. Matter Mater. Phys.*, 1975, **12**, 15–19.
- N. S. McIntyre and D. G. Zetaruk, *Anal. Chem.*, 1977, **49**, 1521–1529.
- S. Marik, D. Singh, B. Gonano, F. Veillon, D. Pelloquin and Y. Bréard, *Scr. Mater.*, 2020, **186**, 366–369.
- B. Martínez, F. Sandiumenge, A. Rouco, A. Labarta, J. Rodríguez-Carvajal, M. Tovar, M. T. Causa, S. Galí and X. Obradors, *Phys. Rev. B: Condens. Matter Mater. Phys.*, 1992, **46**, 10786–10792.
- D. Sherrington, *J. Phys. A: Math. Gen.*, 1978, **11**, L185–L188.
- S. Shtrikman and E. P. Wohlfarth, *Phys. Lett. A*, 1981, **85**, 467–470.
- M. Ikeda and M. Aniya, *J. Non-Cryst. Solids*, 2013, **371**–372, 53–57.
- A. Kumar, R. P. Tandon and V. P. S. Awana, *J. Magn. Magn. Mater.*, 2014, **349**, 224–231.
- J. A. Mydosh, *Spin Glasses*, CRC Press, 2014, p. 280.
- S. F. Jin, Q. Huang, Z. P. Lin, Z. L. Li, X. Z. Wu, T. P. Ying, G. Wang and X. L. Chen, *Phys. Rev. B: Condens. Matter Mater. Phys.*, 2015, **91**, 094420.
- T. Wright, Y. Prots and M. Valldor, *Chem. – Eur. J.*, 2016, **8**, 11303–11309.
- T. Chakrabarty, A. V. Mahajan and S. Kundu, *J. Phys.: Condens. Matter*, 2014, **26**, 405601.
- B. Almoussawi, H. Tomohiri, H. Kageyama and H. Kabbour, *Eur. J. Inorg. Chem.*, 2021, 1271–1277.

